Inorganic Chemistry

pubs.acs.org/IC Article

Artificial Iron Proteins: Modeling the Active Sites in Non-Heme Dioxygenases

Kelsey R. Miller, Jonathan D. Paretsky, Alec H. Follmer, Tillmann Heinisch, Kaustuv Mittra, Sheraz Gul, In-Sik Kim, Franklin D. Fuller, Alexander Batyuk, Kyle D. Sutherlin, Aaron S. Brewster, Asmit Bhowmick, Nicholas K. Sauter, Jan Kern, Junko Yano, Michael T. Green, Thomas R. Ward, and A. S. Borovik*

Cite This: https://dx.doi.org/10.1021/acs.inorgchem.9b03791 Read Online

ABSTRACT: An important class of non-heme dioxygenases contains a conserved Fe binding site that consists of a 2-His-1-carboxylate facial triad. Results from structural biology show that, in the resting state, these proteins are six-coordinate with aqua ligands occupying the remaining three coordination sites. We have utilized biotin−streptavidin (Sav) technology to design new artificial Fe proteins (ArMs) that have many of the same structural features found within active sites of these non-heme dioxygenases. An Sav variant was isolated that contains the $S_{112}E$ mutation, which installed a carboxylate side chain in the appropriate position to bind to a synthetic Fe^{II} complex confined within Sav. Structural studies using X-ray diffraction (XRD) methods revealed a facial triad binding site that is composed of two N donors from the biotinylated ligand and the monodentate coordination of the carboxylate from $S_{112}E$. Two aqua ligands complete the primary coordination sphere of the Fe^{II} center with both involved in hydrogen bond networks within Sav. The corresponding Fe^{III} protein was also prepared and structurally characterized to show a six-coordinate complex with two exogenous acetato ligands. The Fe^{III} protein was further shown to bind an exogenous azido ligand through replacement of one acetato ligand. Spectroscopic studies of the ArMs in solution support the results found by XRD.

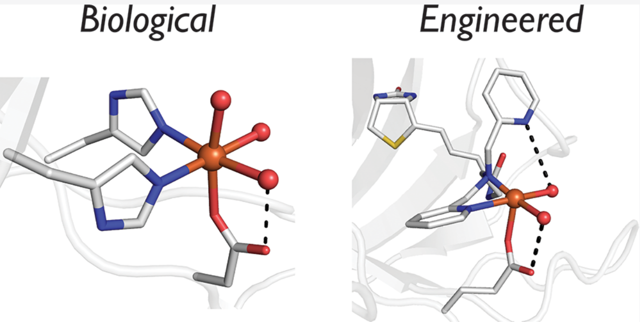

■ INTRODUCTION

Mononuclear non-heme Fe oxygenases are enzymes that catalyze a wide range of oxidative transformations using dioxygen as the terminal oxidant.[1−7] Many of these enzymes share a common Fe binding site that is composed of side chains from two histidine residues and either a glutamate or aspartate amino acid residue.[8−10] This endogenous binding site coordinates an Fe center in a facial manner and is referred to as the 2-His-1-carboxylate facial triad.[11] Information from structural biology indicates that in the Fe^{II} resting state of these proteins, and in the absence of any exogenous cofactors, the remaining coordination sites are occupied by water molecules (Figure 1).[12−14] A common feature of these structures is the presence of an intramolecular hydrogen bond (H-bond) between one of the aqua ligands and the carbonyl group of the coordinated carboxylate ligand.

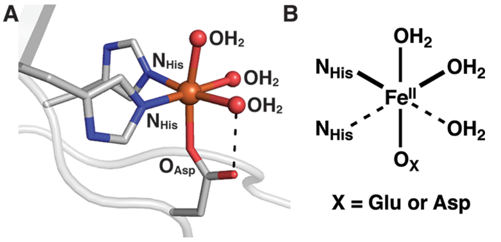

Figure 1. Fe binding site in cephalosporin synthase showing the 2-His-1-carboxylate facial triad (**A**, PDB: 1RXF) and a ChemDraw version of the active site (**B**).

Attempts to model this type of coordination environment include synthetic systems that catalyze the epoxidation and/or cis-dihydroxylation of olefins with H_2O_2 and O_2[15,16] and the intramolecular arene hydroxylation of benzoylformate with O_2.[17−19] However, it has proven challenging to develop synthetic complexes whose coordination spheres resemble those found within these proteins. For instance, reported complexes that emulate the facial triad have been derived from sterically hindered N donors and terphenylcarboxylate ligands[20] and tripodal ligands[21−30] but lack the aqua ligands found within protein active sites. In addition, these systems do

Received: December 31, 2019

not replicate the control over the secondary coordination spheres that is seen within metalloproteins.

We have utilized a complementary approach to develop biorelevant Fe active sites that combine synthetic inorganic chemistry and protein engineering to design artificial metalloproteins (ArMs).[31−37] The approach capitalizes on biotin−streptavidin (Sav) technology to predictably insert biotinylated synthetic complexes into variants of Sav.[38−41] We reasoned that these protein hosts could provide ligands within the primary coordination sphere and simultaneously influence the secondary coordination sphere to better emulate natural active sites. Moreover, these constructs would be stable in aqueous solution allowing for water to act as a ligand, as is found in natural metalloproteins. Our previous work has shown how the primary coordination sphere can be manipulated to produce ArMs that model the properties in cupredoxins through engineering an endogenous thiolate ligand into Sav that forms a strong covalent bond to the Cu centers.[42] Moreover, we have demonstrated that Sav can regulate the secondary coordination sphere around a Cu−hydroperoxido complex using intramolecular H-bonding networks.[43] In this report, we describe the design and development of new artificial Fe proteins that simulate the 2-His-1-carboxylate facial triad active site in nonheme monooxygenases. Both primary and secondary coordination spheres of the Fe centers are influenced by the Sav host to produce the new ArMs in which intramolecular H-bonds play a key structural role.

■ RESULTS AND DISCUSSION

Design Concepts, Preparations, and Solution Properties of the Fe ArMs. Previous work in our group found that binding of an endogenous ligand from Sav to a synthetic metallocofactor is possible. Our work on type 1 Cu sites showed how Cu−S_{thiolate} coordination could be achieved by using a relatively short ethylene linker between the biotin and synthetic complex that positioned the Cu center close to the residue at position 112.[42] We reasoned that Fe complexes prepared from a similar construct, bis(2-pyridylmethyl)amine (Figure 2; biot-et-dpa), may also place the metal center near this residue. Introduction of a $S_{112}E$ mutation in Sav would produce a variant that could then promote Fe−$O_{\mathrm{carboxylate}}$ bond formation. In addition, the Sav host was re-engineered to incorporate two additional mutations, $K_{121}A/E_{101}Q$, as described previously.[44] The parent protein host is referred to as 2xm-Sav, and the specific protein host used to develop mononuclear Fe sites is denoted 2xm-$S_{112}E$-Sav.

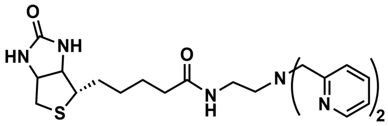

Biot-et-DPA

Figure 2. Biotinylated ligand used in this study.

The biotinylated biot-et-dpa construct was prepared via a three-step route from dpa (Scheme S1) using a modified literature procedure.[42] Formation of the Fe^{II} complex was achieved by treating biot-et-dpa with $FeBr_2$ in CH_3CN under an inert atmosphere to afford $[Fe^{II}(\text{biot-et-dpa})(OH_2)_2]Br_2$. Synthesis of the Fe^{III} complex was accomplished by allowing biot-et-dpa to react with $FeCl_3{\cdot}6H_2O$ in EtOH to yield $[Fe^{III}(\text{biot-et-dpa})(OH_2)_3]Cl_3$. The ArMs containing the Fe^{II} complex $[Fe^{II}(\text{biot-et-dpa}(OH_2)_2(\kappa^1\text{-}O_{E112})\subset\text{2xm-}S_{112}E\text{-Sav}]$ (**1**, eq 1) and the corresponding Fe^{III} complex $[Fe^{III}(\text{biot-et-dpa}(X)_2(\kappa^1\text{-}O_{E112})\subset\text{2xm-}S_{112}E\text{-Sav}]$ (**2**, eq 2) were prepared by incubating a water solution of the complexes with 2xm-$S_{112}E$-Sav at pH 8 in phosphate buffer (50 mM) or at pH 6 in acetate buffer (100 mM). The 2xm-$S_{112}E$-Sav variant is a homotetramer, and to ensure complete binding of the Fe complexes, a 2-(4′-hydroxyazobenzene)benzoic acid (HABA) assay was performed on each ArM.[45] These studies indicated a 4:1 ratio of biotinylated Fe complex to protein host for each ArM that confirmed complete occupancy within the Sav homotetramer (Figure S1).

$$[Fe^{II}(\text{biot-et-dpa})(OH_2)_2]Br_2 \xrightarrow[\text{phosphate buffer, } N_2\text{, rt}]{\text{2xm-}S_{112}\text{-Sav}} \underset{\mathbf{1}}{[Fe^{II}(\text{biot-et-dpa})(OH_2)_2(\kappa^1\text{-}O_{E_{112}})\subset\text{2xm-}S_{112}E\text{-Sav}]}$$

$$[Fe^{III}(\text{biot-et-dpa})(OH_2)_3]Cl_3 \xrightarrow[\text{phosphate buffer, rt}]{\text{2xm-}S_{112}\text{-Sav}} \underset{\mathbf{2}}{[Fe^{III}(\text{biot-et-dpa})(X)_2(\kappa^1\text{-}O_{E_{112}})\subset\text{2xm-}S_{112}E\text{-Sav}]}$$

$$X = OH_2,\ OAc^-$$

Electronic absorbance and EPR spectroscopies were used to characterize **1** and **2** in solution. For **1**, one feature at $\lambda_{\max}$ (ε_M, M^{-1} cm^{-1}) = 375 (700) nm was observed with the band arising from a pyridine to Fe^{II} charge transfer transition (Figure S2A). For **2**, three absorbance bands were found at $\lambda_{\max}$ (ε_M, M^{-1} cm^{-1}) = 350 (2500), 485 (220), and 650 (50) nm (Figure S2B). The parallel-mode, X-band EPR spectrum for **1** displayed a broad signal with a *g* value at 8.8 that is consistent with a high-spin Fe^{II} species with an $S = 2$ spin ground state (Figure S3A). The perpendicular-mode, X-band EPR spectrum of **2** revealed weak features with *g* values at 9.1 and 4.3 which are consistent with the presence of high-spin Fe^{III} species in a rhombic coordination geometry (Figure S3B). Further details on the magnetic properties of these proteins will be described in a subsequent report.

Structural Characterization of 1. A significant advantage of utilizing biotin-Sav technology in the design of ArMs is the strong tendency of Sav to form crystals, which gives us the ability to obtain molecular structures using X-ray diffraction (XRD) methods. In general, the high affinity of biotin for Sav allows for *in crystallo* preparation of Fe ArMs by incubation of apo-Sav crystals with a solution of biotinlyated Fe complexes. For biotinylated complexes, this soaking method should generate single crystals of Sav that contain one complex per subunit. An added benefit of this approach is that we can explore chemistry performed within a single crystal that can be compared to similar processes in solution.

Single crystals of **1** were prepared by soaking crystals of apo-2xm-$S_{112}E$-Sav with $[Fe^{II}(\text{biot-et-dpa})(OH_2)_2]Br_2$. Its structure was solved to a resolution of 1.47 Å to reveal a mononuclear Fe complex immobilized within each subunit in which the Fe center is coordinated by O atoms from the carboxylate group of $S_{112}E$ bound in a κ^1 fashion and two aqua ligands (Figure 3, Tables 1 and 2, and Tables S1 and S2). Nitrogen donors N1 and N2 from dpa also bind to the Fe center with Fe−N1 and Fe−N2 bond lengths of 1.94 and 2.32 Å. Our structure showed two conformations of the pyridine ring containing N3 (Figure 3A). The major complex (**1a**) was modeled to 70% occupancy, and it was found that this pyridine ring is not coordinated

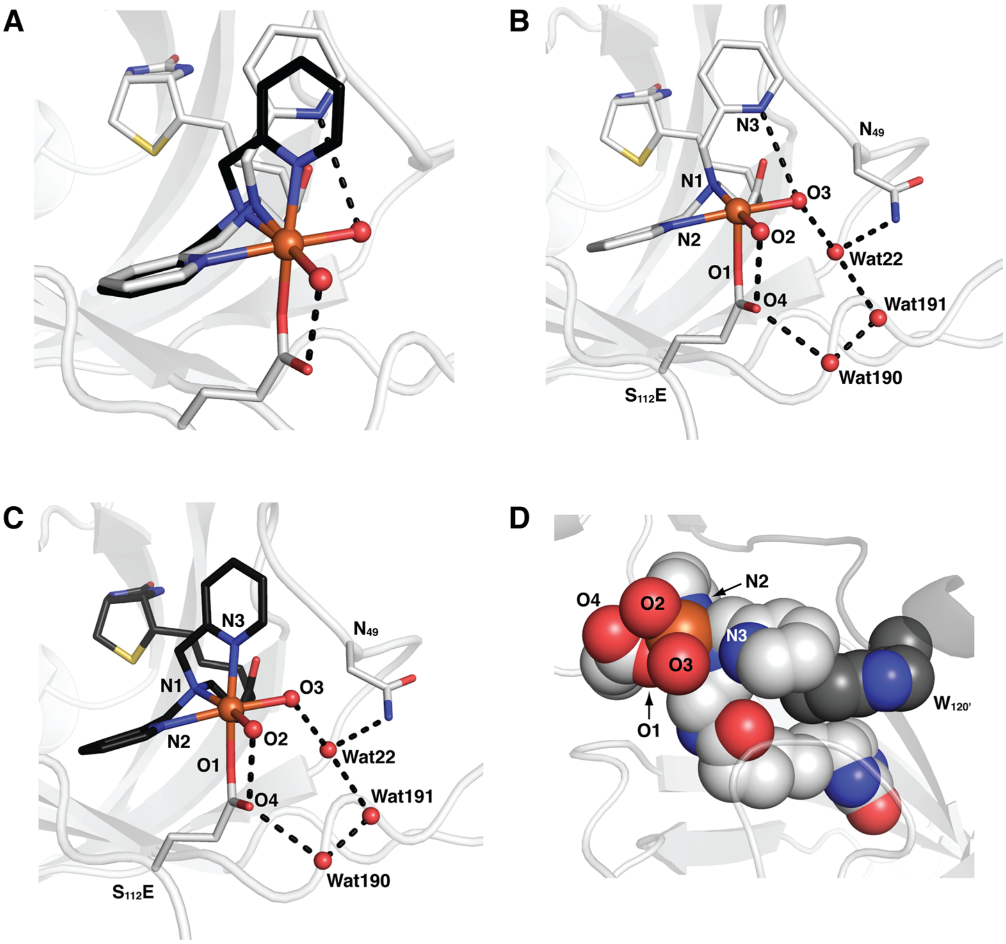

Figure 3. Overlay of the molecular structures of **1a** (gray) and **1b** (black) (A, PDB: 6UIY). The individual molecular structures of **1a** (B) and **1b** (C) and a partial space-filling representation of **1a** highlighting the π-stacking interaction of the biotinylated Fe^{II} complex that includes one of its pyridine rings with W$_{120}$ from the neighboring subunit (**D**, dark gray). Fe ions are colored in orange.

(unbound state); instead, N3 is H-bonded to the aqua ligand of O3. The resultant complex is five-coordinate with a square-pyramidal geometry and a τ value of 0.05 (Figure 3B). The minor complex (**1b**) that was modeled to 30% occupancy is six-coordinate in which N3 is bound to the Fe center (bound state) with an Fe−N3 bond length of 2.21 Å and N2−Fe−N3 and N3−Fe−O3 bond angles of 107 and 79° (Figure 3C). The carboxylate group at S$_{112}$E also has two conformations. In this case, the major confirmation placed O1 in a position to coordinate to the Fe center and was modeled to 80% occupancy (Figure S4A). The minor species has the carboxylate not coordinated to the Fe center and has a 20% occupancy (Figure S4A).

The molecular structure of **1a** revealed an Fe site with a facial arrangement of two N atom donors from dpa and the O atom from the residue of S$_{112}$E which is similar to that of the 2-His-1-carboxylate facial triad observed in all non-heme monooxygenases. In addition, the κ^1 coordination of the glutamate residue in **1a**,**b** leaves O4 positioned to H-bond with the aqua ligand of O2, as gauged by the O4···O2 distance of 2.71 Å. This type of monodentate carboxylate coordination to Fe with an additional intramolecular H-bond is seen in several native nonheme enzymes, such as deacetoxy-cephalosporin C synthase (Figure 1A),[12] phenylalanine hydroxylase binary enzyme (PDB: 1J8U),[46] and soybean lipoxygenase (PDB: 1JNQ).[14] These enzymes have O···O distances that range between 2.5 and 3.6 Å. The structures of the Fe^{II} complex in **1** and Fe^{II} sites in natural enzymes also share the coordination of multiple coordinated water molecules to their Fe^{II} centers.

The 2xm-S$_{112}$E-Sav host in **1** also promotes other non-covalent interactions with the artificial Fe cofactor. For instance, the aqua ligand with O2 has an additional H-bond that involves a structural water molecule (Wat22) that is also H-bonded to the residue of N$_{49}$ and the backbone carbonyl of A$_{86}$. This aqua ligand thus participates in two H-bonds, which could account for the slightly longer Fe−O3 bond length of 2.22 Å in comparison to that found for the Fe−O2 bond (2.17 Å). These water molecules are also part of a larger H-bonding network that extends from N3 to the glutamate 112 side chain and helps in stabilizing its coordination to the Fe center (Figures 3B,C). Furthermore, the noncoordinating pyridine ring participates in an additional π-stacking interaction with the residue of W$_{120}$ from the adjacent subunit with a centroid$_{py}$−centroid$_{trp}$ distance of 4.86 Å that likely contributes to the stabilization of this conformation (Figure 3D).

In synthetic complexes, dpa binds solely as a tridentate ligand to Fe$^{II/III}$ centers. In fact, analysis of all the structures in the Cambridge Structural Database[47] for complexes containing Fe(dpa) fragments (over 300 entries) found that both pyridine N atoms are bound to the Fe center in the crystalline phase. Confinement of [Fe^{II}(biot-et-dpa)(OH$_2$)$_2$]Br$_2$ within 2xm-S$_{112}$E-Sav appears to promote the unusual bidentate coordi-

Table 1. Selected Bond Lengths (Å) and Angles (deg) for the ArMs from XRD Measurements

	1a	1b	2	2-N_3
Fe−O1	2.16	2.16	2.11	2.35
Fe−O2	2.17	2.17	2.17	2.00
Fe−O3	2.22	2.22	2.15	
Fe−N1	1.94	2.31	2.15	2.27
Fe−N2	2.32	2.36	2.23	2.52
Fe−N3		2.21	2.18	2.27
Fe−N4				2.15
N1−Fe−O2	167	167	167	169
N1−Fe−N2	79	67	71	79
N2−Fe−O3	170	164	165	
O2−Fe−O3	91	91	96	
O1−Fe−1	100	91	90	95
O1−Fe−N2	82	78	79	75
O1−Fe−N3		166	164	146
O1−Fe−O2	91	91	96	87
O1−Fe−O3	92	92	95	
N1−Fe−N3		79	76	83
N2−Fe-N3		107	104	71
N3−Fe−O2		101	100	89
N3−Fe−O3		79	78	
O1−Fe−N4				110
O2−Fe−N4				89
N1−Fe−N4				101
N2−Fe−N4				175
N3−Fe−N4				103
Fe−N4−N5				120

Table 2. Selected H Bonds (Å) for the ArMs from XRD Measurements

distance	1	2	2-N_3
N3···O3	3.51		
O3···Wat22	2.54		
Wat22···N_{49}	3.00		
Wat22···Wat191	3.05		
Wat191···Wat190	2.34		
Wat190···O4	3.12		
O4···O2	2.71		
O6···N_{49}		2.97	
N4···Wat1			2.88
Wat1···N_{49}			3.17

nation of dpa. The trapping of this Fe^{II} species with a noncoordinating pyridine ligand highlights the importance of the local environment around a metal center and how it can influence the structure of the embedded metal complex.

Structural Characterization of biot-et-dpa$\subset$2xm-S_{112}E-Sav. The unusual molecular structure of the Fe complexes in **1** prompted us to examine the structure of 2xm-S_{112}E-Sav containing just biot-et-dpa. We were interested in determining how the dpa ligand was positioned within the protein host in the absence of the Fe center and to examine if any structural differences occurred upon coordination to Fe. The structure of biot-et-dpa$\subset$2xm-S_{112}E-Sav was solved to a resolution of 1.35 Å, and both the dpa ligand and carboxylate group at position 112 were modeled with single conformations at 100% occupancy (Figure 4A and Tables S1 and S2). Both N1 and N2 are centered near the carboxylate group at position 112, and the pyridine ring containing N3 adopts a confirmation nearly identical with what is found in **1a**, including the same π-stacking interaction with W_{120} (Figure 4C). Additional noncovalent interactions are present in the form of an extended H-bonding network that includes N1 and N3, a series of water molecules, and the side chains of N_{49} and S_{112}E (Figure 4A). Atom N3 thus forms a H-bond as in **1a** but with a structural water molecule rather than an aqua ligand. Notice that the H-bonding network also links N3 to the carboxylate group at S_{112}E, which influences its orientation.

The structure found of biot-et-dpa$\subset$2xm-S_{112}E-Sav provided insights on how the protein host influences both the primary and secondary coordination spheres in **1** (Figure 4A,B). The glutamate and pyridine with N3 have two different conformations in the structure of **1** (Figure S4A). For the glutamate, the minor state in **1** has the carboxylate occupying the same position as that observed in biot-et-dpa$\subset$2xm-S_{112}E-Sav that places O atoms greater than 3.0 Å from the Fe center. In its bound state, the carboxylate group rotates toward the dpa ligand, enabling O1 to coordinate to the Fe center. Moreover, the placement of unbound pyridine in **1a** is only displaced by 0.6 Å from the position occupied by the same ring in biot-et-dpa$\subset$2xm-S_{112}E-Sav. This change appears to be enough to promote intramolecular H-bonding with the aqua ligand of O3 but not enough to coordinate to the Fe center (Figure 4C). For the bound state in **1b**, there is a significant change in the position of the pyridylmethyl arm that results in N3 moving over 2.0 Å in order to coordinate to the Fe^{II} center. There is also an extended H-bonding network like that found in **1** that includes N3, several water molecules, and the S_{112}E side chain (Figure 4C).

Structural Characterization of 2. To evaluate the effects of Fe oxidation on the molecular structure of the active site, we prepared single crystals of **2** by soaking crystals of apo 2xm-S_{112}E-Sav with $[Fe^{III}(\text{biot-et-dpa})(OH_2)_3]Cl_3$. An analysis of crystals that diffracted to a 1.40 Å resolution revealed the formation of a six-coordinate mononuclear Fe complex within each subunit of Sav (Figure 5, Tables 1 and 2, and Tables S3 and S4). The primary coordination sphere is composed of an N_3O_3 donor set with an O atom donor from the residue of S_{112}E that is bound in a κ^1 manner similar to that observed in **1**. The other O atom donors are from acetate ions (from the crystallization conditions) that also bind as monodentate ligands and occupy the same coordination sites as the aqua ligands in **1**. The dpa ligand binds facially to the Fe^{III} center, and all three N donors are coordinated. Notice that the structural water molecule (Wat22) that was found in **1** is not present in **2**, which allows O6 of the acetato ligand to H-bond with the amide residue of N_{49}, with a N_{49}···O6 distance of 2.97 Å.

To evaluate if photoreduction was occurring on the crystals of **2** and the extent of change that would cause on the resultant structure, XRD data were also collected using an X-ray free electron laser (XFEL). This technique utilizes femtosecond X-ray pulses to collect XRD data in a serial fashion with each diffraction image obtained from a new crystal.[48−51] Detection occurs before the diffusion of radicals or solvated electrons that often causes X-ray-induced changes in protein structures. Therefore, this method has provided structural data for metal centers in a nondamaged (that is, not photoreduced) state for several metalloproteins.[48−51] We were able to obtain a molecular structure of **2** that was resolved to 1.50 Å (Tables S3 and S4). The structures of **2** obtained from frozen crystals by XRD and room-temperature crystals with the XFEL

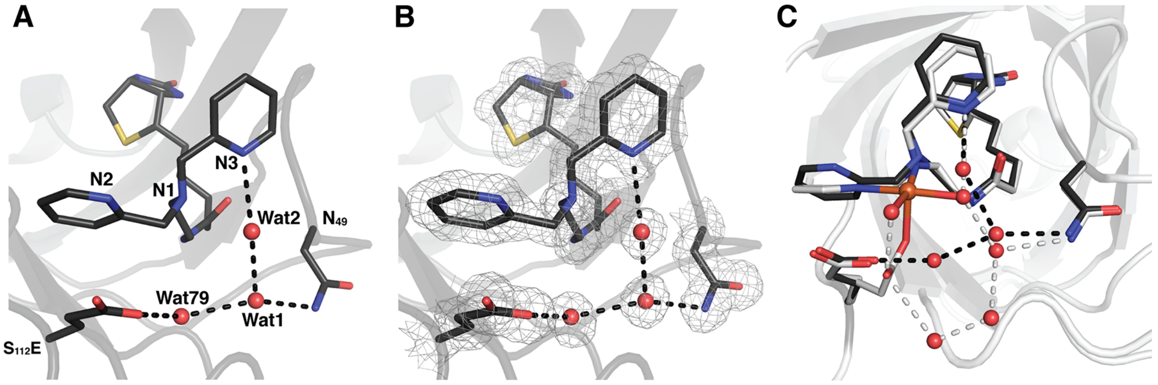

Figure 4. Molecular structure of biot-et-dpa$\subset$2xm-S$_{112}$E-Sav (A, PDB: 6UIU). The $2F_o - F_c$ electron density map (gray, contoured at 1σ) is highlighted in (B) with same labeling as in (A). Overlay of biot-et-dpa$\subset$2xm-S$_{112}$E-Sav (black) and **1a** (gray) (C) that shows the H-bonding networks associated with biot-et-dpa$\subset$2xm-S$_{112}$E-Sav (black dashes) and **1a** (gray dashes). The number schemes in (B) and (C) are the same as in (A).

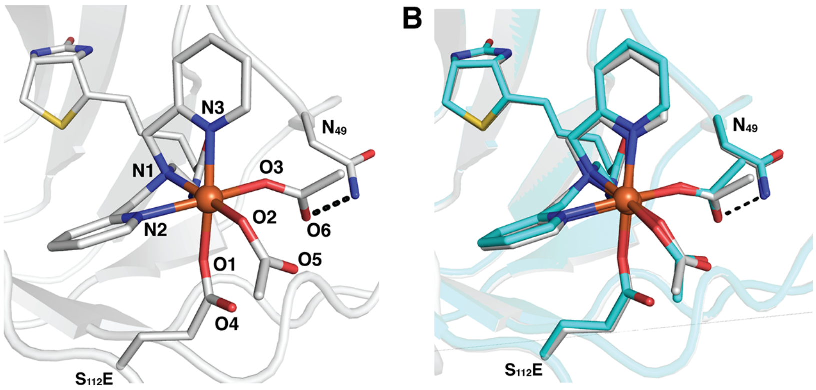

Figure 5. Molecular structure of **2** (A, PDB: 6UIO) and an overlay of the structure collected using XFEL (B, carbons colored in teal, PDB: 6US6). The number scheme in (B) is the same as in (A).

produced the molecular structures that were identical (Figure S4D) with an average difference in the Fe−N/O bond lengths of 0.03 Å. Notice that there is a slight difference in the orientations of the ligands in the two structures (Figure 5B), which could be caused by the different temperatures that were used for data collection. Nevertheless, these results suggest that the structure of **2** obtained using synchrotron radiation at cryogenic temperatures had only limited radiation damage.

X-ray Absorption Spectroscopy. The properties of the Fe center in **1** were further probed using X-ray absorption spectroscopy (XAS) to gain a better understanding of the structure of the protein-embedded complex in solution (see Figures S5−S7 in the Supporting Information). X-ray absorption near-edge structure (XANES) analysis provided an energy edge for **1** at 7122.4 eV (Figure S7), which is consistent with an Fe^{II} center.[52−54] Extended X-ray absorption fine structure (EXAFS) analysis revealed that for **1** there are five O/N scatterers at a distance of 2.15 Å (Table 3 and Tables S5 and S6). Two additional shells from the Fe center were fit to four carbon scatterers at 3.01 Å and one at 2.63 Å. The longer distance carbon scatterers could include the carbonyl C atom of the S$_{112}$E side chain which is found at an Fe···C distance of 3.12 Å by XRD. The shorter Fe···C distance of 2.60 Å matched that found by XRD for the Fe center to the methylene carbon of the unbound pyridylmethyl group. Taken together, these data suggest that the predominate species in solution for **1** is also the unbound state in which one pyridine ring of dpa is not coordinated (Figure 3B).

Table 3. Comparison of Metrical Parameters for 1 Obtained by XAS and XRD

bond	no. of scatterers	XAS (Å)	XRD (Å)
av Fe−O/N	5	2.15	2.16
av Fe···C	4	3.01	3.01
Fe···C$_{\text{methylene}}$	1	2.63	2.60

Azide Binding to 2. We chose to examine the binding of azide ions to **2** in order to investigate how exogenous ligands bind to the Fe center. In solution studies, **2** was treated with a 100-fold excess of NaN$_3$ in pH 6 acetate buffer to afford a new spectrum with a band at a $\lambda_{\max}$ (ε_M, M^{-1} cm^{-1}) = 405 (3000) nm that is assigned to an azido to Fe^{III} charge transfer transition (Figure 6A and Figure S8).[55] Parallel *in crystallo* studies were performed that involved soaking crystals of **2** in a 100 mM solution of NaN$_3$ to afford **2-N$_3$**, whose structure was obtained to a resolution of a 1.85 Å (Figure 6B,C). Analysis of the molecular structure of **2-N$_3$** revealed a monomeric Fe complex where the dpa ligand, the carboxylate side chain of S$_{112}$E, and one acetato ligand containing O3 are coordinated in the same positions as found in **2** (Figure 6B,C). However, the second acetato ligand is absent. In its place is electron density that we have modeled as a terminal azido ligand with an Fe−N4 bond length of 2.15 Å. The azido ligand has an Fe−N4−N5 bond angle of 120.1° that is comparable to bond angles found in previously reported Fe^{III}-N$_3$ complexes.[56] The

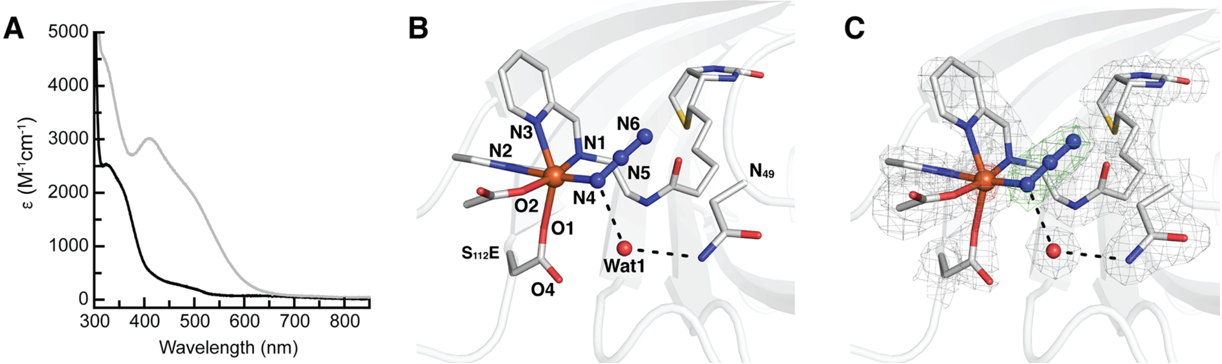

Figure 6. Electronic absorbance spectra of **2** (black) and **2-N$_3$** (gray) recorded at 4 °C in 100 mM acetate buffer pH 6 (A). Molecular structure of **2-N$_3$** (B, PDB: 6UIZ), and the 2F_o − F_c electron density map (gray, contoured at 1σ), F_o − F_c omit map (green, contoured at 3σ), and anomalous difference density (red, contoured at 5 σ) are shown in (C). The numbering scheme in (C) is the same as in (B).

presence of the azido ligand in **2-N$_3$** causes an 0.29 Å elongation of the Fe−N2 bond distance comparable to what is observed in **2**, which is consistent with an azido ligand having a stronger trans influence than an acetate ion. The structural water molecule Wat1 is modeled at 100% occupancy and is part of an H-bonding network that includes the azido ligand. The H-bonding network extends from the proximal N4 of the azido ligand and includes Wat1 and the amide residue of N$_{49}$ with N4···Wat1 and Wat1···N$_{49}$ distances of 2.88 and 3.17 Å, respectively (Figure 6B). From this structure, it unclear whether the N4···Wat1 interaction contributes to the orientation of the azido ligand—most likely, steric interactions among the azido ligand, the dpa ligand, WAT1, and the neighboring side chains dominate.

SUMMARY AND CONCLUSIONS

The results from these studies on our new Fe proteins further illustrates the versatility of using biotin-Sav technology to engineer ArMs. Our approach leverages the proper placement of synthetic complexes proximal to endogenous functional groups to produce new biomimetic constructs. We utilized knowledge gained from our previous work on Cu proteins, which revealed that an ethylene linker between a metal complex and the biotin positioned the Cu center near the side chain at position 112. Following this design concept, the Sav protein was re-engineered to produce the host 2xm-S$_{112}$E-Sav, which included a glutamate at position 112. When it was matched with the biotinylated complexes [Fe^{II}(biot-et-dpa)(OH$_2$)$_2$]Br$_2$ and [Fe^{III}(biot-et-dpa)(OH$_2$)$_3$]Cl$_3$, ArMs were produced with properties that resemble those found in mononuclear non-heme iron enzymes. The positioning of the artificial cofactors within 2xm-S$_{112}$E-Sav allow for monodentate coordination of the carboxylate side chain in a manner identical with that found in the active sites of Fe monooxygenases. Moreover, the unusual structural finding in **1a**, in which one pyridine group of the dpa ligand is not coordinated, produced an Fe binding that is similar to the 2-His-1-carboxylate facial triad found in the natural metalloproteins. The observation that only one pyridine group is coordinated to the Fe center in **1a** is unusual and has not been structurally observed in other Fe complexes with dpa. We attribute this difference to the confinement of the complex within a protein host that helps regulate the secondary coordination sphere around the Fe complexes. In fact, there are several noncovalent interactions to the complexes which include those with a pyridine ring of the dpa ligand that stabilizes the unbound state found in **1a**. An additional H-bond was found between an aqua ligand and the noncoordinating O atom of a glutamate side chain, an interaction that is found in many nonheme Fe enzymes.

The structure of **2** also revealed a κ^1 coordination to the Fe^{III} center of the carboxylate at position 112. In **2**, the Fe complex is six-coordinate and the aqua ligands have been replaced with acetato ligands to produce a primary coordination sphere that contains three monodentate carboxylate ligands. Again, H-bonds involving the carboxylate ligands appear to help stabilize this unusual coordination environment. Substitution of the one of the acetato ligands was achieved by treating **2** with excess azide ion to produce **2-N$_3$**. The structure of **2-N$_3$**, along with those of **1** and **2**, also illustrates the importance of the amide side chain of N$_{49}$ in maintaining H-bonding networks around the complexes. When they are taken together, our findings highlight how the synergistic design of Sav and an artificial metallocofactor allow for the control of both the primary and secondary coordination spheres of a confined metal complex within a protein host. This control, along with the similarity of the Fe^{II} site in **1** to those of nonheme oxygenases, provides us the opportunity to probe oxidative processes including binding of dioxygen. Such studies are ongoing.

EXPERIMENTAL SECTION

General Methods. All commercially available reagents were obtained of the highest purity and were used as received. Acetonitrile (CH_3CN), ethanol (CH_3CH_2OH), and diethyl ether were degassed with argon and dried by vacuum filtration through activated alumina according to the procedure by Grubbs.[57] Triethylamine was distilled from KOH. Thin-layer chromatography (TLC) was performed on Merck 60 F254 aluminum-backed silica plates or Merck 60 F254 glass-backed basic aluminum oxide plates. Eluted plates were visualized using UV light. Silica or basic alumina gel chromatography was performed with the indicated solvent system using Fisher reagent silica gel 60 (230−400 mesh) or Sigma reagent Brockmann 1 basic aluminum oxide 58 (150 mesh). Biotin pentafluorophenol ester (biot-PFP)[58] and bis(2-picolyl)amine[59] were prepared according to literature procedures.

2-(2-(Bis(pyridin-2-ylmethyl)amino)ethyl)isoindoline-1,3-dione (1).[42] dpa (2.03 g, 10.0 mmol), bromoethylphthalimide (2.93 g, 11.0 mmol), KI (0.339 g, 0.002 mol), and K_2CO_3 (5.6 g, 41 mmol) were dissolved in 60 mL of acetonitrile and refluxed for 24 h. The solution was cooled to room temperature, filtered, and reduced to dryness. The maroon-brown residue was dissolved in 30 mL of dichloromethane and washed with 3 × 30 mL of aqueous $NaHCO_3$ (with a small addition of brine) and 2 × 30 mL of water. The maroon-brown organic layer was acidified with 20 mL of 12 mM HCl dissolved in 10 mL of water and washed with 5 × 30 mL of dichloromethane. The aqueous layer was carefully neutralized with solid $NaHCO_3$ and extracted with 4 × 30 mL of dichloromethane. The solution was dried with $MgSO_4$, filtered, and reduced to dryness to yield a red-brown oil. The crude product was purified via column chromatography with silica gel and methanol/dichloromethane/Et_3N (9/90/1) or with basic alumina and methanol/dichloromethane (10/90) as the eluent to yield pure **1** as a yellow oil (1.68 g, 44%−50%). ^1H NMR (500 MHz, $CDCl_3$): δ 8.44 (d, 2H), 7.82 (dd, 2H), 7.74 (dd, 2H) 7.42 (t, 2H), 7.34 (d, 2H), 7.06 (t, 2H), 3.85 (m, 6H), 2.86 (t, 2H). MS (ESI, MeOH): m/z calcd $C_{22}H_{20}N_4O_2$ [M + (Na^+)] 395.15, found 395.09.

***N*,*N*-Bis(pyridin-2-ylmethyl)ethane-1,2-diamine (2).**[42] Hydrazine monohydrate (1.10 mL, 0.020 mol) and **1** (1.7 g, 5.0 mmol) were dissolved in 60 mL of ethanol and refluxed under N_2 for 3 h. The phthalhydrazide byproduct precipitated as a white solid after 15 min of reflux. The solution was filtered to remove the phthalhydrazide and washed with 3 × 5 mL of chloroform. The solution was reduced to dryness, and the yellow oily residue was dissolved in 40 mL of chloroform and 40 mL of 1 M NaOH. The aqueous layer was extracted with 3 × 40 mL of chloroform, dried over $MgSO_4$, filtered, and reduced to dryness. The product **2** was recovered as a yellow oil (0.80 g, 77%). ^1H NMR (500 MHz, $CDCl_3$): δ 8.53 (d, 2H), 7.66 (t, 2H), 7.50 (d, 2H) 7.15 (t, 2H), 3.85 (s, 4H), 2.80 (t, 2H), 2.66 (t, 2H). MS (ESI, MeOH): m/z calcd $C_{14}H_{18}N_4$ [M + (H^+)] 243.16, found 243.11.

Biot-ethyl-dpa (3).[42] A solution of biot-PFP (1.30 g, 3.01 mmol), **2** (0.85 g, 3.0 mmol), and triethylamine (0.39 g, 3.0 mmol) in 20 mL of DMF was stirred overnight. The DMF was removed under vacuum to yield a sticky tan residue. The residue was triturated with diethyl ether until a free-flowing solid formed (3−7 days). The light tan solid was filtered, washed with diethyl ether, and dried under vacuum (1.49 g, 91%). The solid **3** was stored under an inert atmosphere. ^1H NMR (500 MHz, DMSO): δ 8.44 (d, 2H), 7.75 (br, 1H), 7.71 (t, 2H) 7.50 (d, 2H), 7.21 (t, 2H), 6.40 (s, 1H), 6.33 (s, 1H), 4.27 (t, 1H), 4.07 (t, 1H), 3.72 (s, 4H), 3.16 (q, 2H), 3.04 (q, 1 H), 2.78 (dd, 1 H), 2.55 (s, 1H), 2.46 (t, 2H), 2.02 (t, 2H), 1.45 (m, 6H). MS (ESI, MeOH): m/z calcd $C_{24}H_{32}N_6O_2S$ [M + (Na^+)] 491.22, found 491.17.

Preparation of Metal Complexes. *[Fe^{II}(biot-ethyl-dpa)(OH_2)$_2$]Br_2.*[60] [Fe^{II}(Biot-ethyl-DPA)(OH_2)$_2$]Br_2 was prepared by addition of **3** (53 mg, 0.24 mmol) in 10 mL of acetonitrile to $FeBr_2$. A pale yellow solid immediately precipitated from the solution. The suspension was stirred under N_2 for 30 min, after which the pale yellow solid was collected via filtration, washed with CH_3CN/diethyl ether (1/1), and dried under vacuum (0.125 g, 75%). The solid was stored under an inert atmosphere. HR-MS (ESI, 1% DMF/MeCN): m/z calcd for $C_{24}H_{32}FeN_6O_2SBr$ [M − (Br^-)] 603.08, found 603.08. Anal. Calcd for $C_{24}H_{36}N_6SO_4FeBr_2$: C, 40.02; H, 5.04; N, 11.67. Found: C, 39.67; H, 4.52; N, 11.38.

[Fe^{III}(biot-ethyl-dpa)(OH_2)$_3$]Cl_3.[61] [Fe^{III}(Biot-ethyl-DPA)(OH_2)$_3$]Cl_3 was prepared by addition of **3** (0.09 g, 0.2 mmol) in 3 mL of ethanol to $FeCl_3 \cdot 6H_2O$ (0.10 g, 0.38 mmol) in 3 mL of ethanol. A yellow solid immediately precipitated from the solution. The suspension was stirred under N_2 for 15 min, after which the yellow solid was isolated via filtration. The solid was washed with 10 mL of chilled ethanol/ether (4/1) and dried under vacuum (0.10 g, 86%). The solid was stored under an inert atmosphere. HR-MS (ESI, MeOH): m/z calcd for $C_{24}H_{32}Cl_2FeN_6O_2S$ [M − (Cl^-)] 594.10, found 594.08. Anal. Calcd for $C_{24}H_{38}N_6SO_5FeCl_3$: C, 42.09; H, 5.59; N, 12.27. Found: C, 42.28; H, 5.12; N, 12.23.

Analytical and Spectroscopic Methods. *HABA Titrations.* To 2.4 mL of 8 μM Sav in 200 mM sodium phosphate buffer at pH 7 was added 300 μL of 10 mM 2-(4′-hydroxyazobenzene)benzoic acid (HABA) in 200 mM phosphate buffer pH 7. After 5 min equilibration, the absorbance at 506 nm was recorded. A solution of 1 mM Fe complex in nanopure water was added in 4−20 μL portions until approximately 4 equiv had been added. The absorbance at 506 nm was recorded until no further changes in intensity were observed.

Electronic Absorption Studies. A solution of lyophilized protein (50−250 μM) was prepared in nanopure water. Four equivalents of Fe complex (0.2−1 mM) in nanopure water was added to the protein solution. Samples were diluted to their final concentrations in a final volume of 500 μL containing 50 mM potassium phosphate or 100 mM sodium acetate buffer at the indicated pH.

EPR Studies. A solution of protein (500 μM) was prepared in nanopure water. Four equivalents of Fe complex (2 mM) in nanopure water was added to the protein solution. Samples were diluted to their final concentrations in a final volume of 300 μL containing 50 mM potassium phosphate or 100 mM sodium acetate buffer at the indicated pH. The sample was transferred to an EPR tube and frozen at 77 K in liquid nitrogen and the measurement run at 10 K.

XAS Studies. A solution of protein (750 μM) was prepared in nanopure water. Four equivalents of Fe complex (3 mM) in nanopure water was added to the protein solution. Samples were diluted to their final concentrations in a final volume of 250 μL with nanopure water. The sample was then poured in liquid ethane to freeze and packed as a solid into a precooled XAS sample holder.

Protein Crystallization. *Crystallization of [Fe^{II}(biot-et-dpa-(OH_2)$_2$(κ^1-O_{E112})⊂2xm-S_{112}E-Sav].* Apo-Sav protein was crystallized by the sitting drop vapor diffusion method under an inert atmosphere. Diffraction-quality crystals were grown at room temperature by mixing 3.5 μL of protein solution (26 mg/mL lyophilized protein in water) and 1.5 μL of crystallization buffer (2.0 ammonium sulfate, 0.1 M sodium acetate, pH 4). The droplet was equilibrated against a reservoir solution of 100 μL of crystallization buffer. Single crystals of Sav were prepared by soaking apo crystals in a soaking buffer (2.6 M ammonium sulfate, 0.1 M sodium acetate, pH 8) with a 10 mM stock solution of [Fe^{II}(Biot-et-DPA)(OH_2)$_2$]Br_2 in nanopure water (9 μL of crystallization buffer, 1 μL of [Fe^{II}(biot-et-dpa)(OH_2)$_2$]Br_2) overnight. After the soaking, crystals were transferred to cryoprotectant for 1 min (30% glycerol in crystallization buffer) and shock-frozen in liquid nitrogen.

Crystallization of [Fe^{III}(biot-et-dpa(OAc)$_2$(κ^1-O_{E112})⊂2xm-S_{112}E-Sav]. Apo-Sav protein was crystallized by the sitting drop vapor diffusion method. Diffraction-quality crystals were grown at room temperature by mixing 3.5 μL of protein solution (26 mg/mL lyophilized protein in water) and 1.5 μL of crystallization buffer (2.0 ammonium sulfate, 0.1 M sodium acetate, pH 4). The droplet was equilibrated against a reservoir solution of 100 μL of crystallization buffer. Single crystals of Sav were prepared by soaking apo crystals in a soaking buffer (2.6 ammonium sulfate, 0.1 M sodium acetate, pH 6) with a 10 mM stock solution of [Fe^{III}(biot-ethyl-dpa)(OH_2)$_3$]Cl_3 in nanopure water (9 μL crystallization buffer, 1 μL [Fe^{III}(biot-ethyl-dpa)(OH_2)$_3$]Cl_3) overnight. After the soaking, crystals were transferred to cryoprotectant for 1 min (30% glycerol in crystallization buffer) and shock-frozen in liquid nitrogen. Crystals were prepared in the same manner for data collected using XFEL.

Crystallization of biot-et-dpa⊂2xm-S_{112}E-Sav. Apo-Sav protein was crystallized by the sitting drop vapor diffusion method. Diffraction-quality crystals were grown at room temperature by mixing 3.5 μL of protein solution (26 mg/mL of lyophilized protein in water) and 1.5 μL of crystallization buffer (2.0 ammonium sulfate, 0.1 M sodium acetate, pH 4). The droplet was equilibrated against a reservoir solution of 100 μL of crystallization buffer. Single crystals of Sav were prepared by soaking apo crystals in a soaking buffer (2.6 ammonium sulfate, 0.1 M sodium acetate, pH 6) with a 10 mM stock solution of biot-et-dpa in nanopure water (9 μL of crystallization buffer, 1 μL of biot-et-dpa) overnight. After the soaking, crystals were transferred to cryoprotectant for 1 min (30% glycerol in crystallization buffer) and shock-frozen in liquid nitrogen.

Crystallization of [Fe^{III}(biot-ethyl-dpa)(OAc)(N_3)(κ^1-O_{E112})⊂2xm-S_{112}E-Sav]. Apo-Sav protein was crystallized by the sitting drop vapor diffusion method. Diffraction-quality crystals were grown at room temperature by mixing 3.5 μL of protein solution (26 mg/mL lyophilized protein in water) and 1.5 μL of crystallization buffer (2.0 ammonium sulfate, 0.1 M sodium acetate, pH 4). The droplet was equilibrated against a reservoir solution of 100 μL of crystallization buffer. Single crystals of Sav were prepared by soaking apo crystals in a soaking buffer (2.6 ammonium sulfate, 0.1 M sodium acetate, pH 6) with a 10 mM stock solution of [Fe^{III}(biot-ethyl-dpa)$(OH_2)_3$]Cl_3 in nanopure water (9 μL crystallization buffer, 1 μL [Fe^{III}(biot-ethyl-dpa)$(OH_2)_3$]Cl_3) overnight. After this initial soaking, crystals were again soaked in a soaking buffer (2.6 ammonium sulfate, 0.1 M sodium acetate, pH 6) with a 1 M stock solution of NaN_3 in nanopure water for 5−10 min (9 μL of crystallization buffer, 1 μL of NaN_3). After the second soaking, the crystals were transferred to cryoprotectant for 1 min (30% glycerol in crystallization buffer) and shock-frozen in liquid nitrogen.

Physical Methods. *Instrumentation.* ^{1}H, ^{13}C, and ^{19}F NMR spectra were recorded at 500/600, 125, and 400 MHz, respectively. ^{1}H NMR spectra were reported in ppm on the δ scale and referenced to tetramethylsilane or solvent residual. The data are presented as follows: chemical shift, multiplicity (s = singlet, d = doublet, t = triplet, q = quartet, quin = quintet, m = multiplet, br = broad), and integration. Mass spectra were measured on a MicroMass AutoSpec E, a MicroMass Analytical 7070E, or a MicroMass LCT Electrospray instrument. Electronic absorbance spectra were recorded with a Cary 50 or 8453 Agilent UV−vis spectrophotometer. X-band (9.64 GHz) EPR spectra were recorded on a Bruker spectrometer equipped with Oxford liquid helium cryostats. The quantification of all signals is relative to a CuEDTA spin standard. The concentration of the standard was derived from an atomic absorption standard (Aldrich). For all instruments, the microwave frequency was calibrated with a frequency counter and the magnetic field with an NMR gaussmeter. A modulation frequency of 100 kHz was used for all EPR spectra. The EPR simulation software (SpinCount) was written by our collaborating author Michael P. Hendrich.[62]

■ ASSOCIATED CONTENT

Supporting Information

The Supporting Information is available free of charge at https://pubs.acs.org/doi/10.1021/acs.inorgchem.9b03791.

> Details of X-ray diffraction, XFEL, and XAS data collection and processing and Figures S1−S8, Tables S1−S6, and Scheme S1 as detailed in the text (PDF)

Accession Codes

PDB 6UIY, 6UIU, 6UIO, 6US6, and 6UIZ contain the supplementary crystallographic data for this paper. These data can be obtained free of charge via https://www.rcsb.org/

■ AUTHOR INFORMATION

Corresponding Author

A. S. Borovik − *Department of Chemistry, 1102 Natural Science II, University of California, Irvine, California 92697, United States;* orcid.org/0000-0001-5049-9952; Email: aborovik@uci.edu

Authors

Kelsey R. Miller − *Department of Chemistry, 1102 Natural Science II, University of California, Irvine, California 92697, United States*

Jonathan D. Paretsky − *Department of Chemistry, 1102 Natural Science II, University of California, Irvine, California 92697, United States*

Alec H. Follmer − *Department of Chemistry, 1102 Natural Science II, University of California, Irvine, California 92697, United States;* orcid.org/0000-0002-6244-6804

Tillmann Heinisch − *Department of Chemistry, University of Basel, CH-4002 Basel, Switzerland*

Kaustuv Mittra − *Department of Molecular Biosciences and Biochemistry, University of California, Irvine, California 92697, United States;* orcid.org/0000-0003-2325-1972

Sheraz Gul − *Molecular Biophysics and Integrated Bioimaging Division, Lawrence Berkeley National Laboratory, Berkeley, California 94720, United States*

In-Sik Kim − *Molecular Biophysics and Integrated Bioimaging Division, Lawrence Berkeley National Laboratory, Berkeley, California 94720, United States*

Franklin D. Fuller − *Linac Coherent Light Source, SLAC National Accelerator Laboratory, Menlo Park, California 94025, United States*

Alexander Batyuk − *Linac Coherent Light Source, SLAC National Accelerator Laboratory, Menlo Park, California 94025, United States*

Kyle D. Sutherlin − *Molecular Biophysics and Integrated Bioimaging Division, Lawrence Berkeley National Laboratory, Berkeley, California 94720, United States*

Aaron S. Brewster − *Molecular Biophysics and Integrated Bioimaging Division, Lawrence Berkeley National Laboratory, Berkeley, California 94720, United States*

Asmit Bhowmick − *Molecular Biophysics and Integrated Bioimaging Division, Lawrence Berkeley National Laboratory, Berkeley, California 94720, United States*

Nicholas K. Sauter − *Molecular Biophysics and Integrated Bioimaging Division, Lawrence Berkeley National Laboratory, Berkeley, California 94720, United States*

Jan Kern − *Molecular Biophysics and Integrated Bioimaging Division, Lawrence Berkeley National Laboratory, Berkeley, California 94720, United States;* orcid.org/0000-0002-7272-1603

Junko Yano − *Molecular Biophysics and Integrated Bioimaging Division, Lawrence Berkeley National Laboratory, Berkeley, California 94720, United States;* orcid.org/0000-0001-6308-9071

Michael T. Green − *Department of Chemistry, 1102 Natural Science II and Department of Molecular Biosciences and Biochemistry, University of California, Irvine, California 92697, United States;* orcid.org/0000-0001-8658-8420

Thomas R. Ward − *Department of Chemistry, University of Basel, CH-4002 Basel, Switzerland;* orcid.org/0000-0001-8602-5468

Complete contact information is available at: https://pubs.acs.org/10.1021/acs.inorgchem.9b03791

Notes

The authors declare no competing financial interest.

■ ACKNOWLEDGMENTS

We thank the National Institutes of Health USA (GM120349 to A.S.B., GM101390 to M.T.G., GM110501 to J.Y., GM126289 to J.K., and GM117126 to N.K.S.) for financial support. K.R.M. acknowledges the National Science Foundation Graduate Research Fellowship (NSF-GRFP I.D. 2015203061) for financial support. Use of the Linac Coherent Light Source (LCLS) at the SLAC National Accelerator Laboratory was supported by the U.S. Department of Energy (DOE), Office of Science, Office of Basic Energy Sciences, under Contract No. DE-AC02-76SF00515, and the Advanced Light Source at Lawrence Berkeley National Laboratory (ALS-09183, A.S.B.) for support of this work. Data processing for the XFEL study was performed in part at the National Energy Research Scientific Computing Center, supported by the DOE Office of Science, Contract No. DEAC02-05CH11231.

REFERENCES

(1) Solomon, E. I.; Brunold, T. C.; Davis, M. I.; Kemsley, J. N.; Lee, S.-K.; Lehnert, N.; Neese, F.; Skulan, A. J.; Yang, Y.-S.; Zhou, J. Geometric and Electronic Structure/Function Correlations in Non-Heme Iron Enzymes. *Chem. Rev.* **2000**, *100*, 235−350.

(2) Kal, S.; Que, L. Dioxygen Activation by Nonheme Iron Enzymes with the 2-His-1-Carboxylate Facial Triad That Generate High-Valent Oxoiron Oxidants. *JBIC, J. Biol. Inorg. Chem.* **2017**, *22*, 339−365.

(3) Bruijnincx, P. C. A.; van Koten, G.; Gebbink, R. J. M. K. Mononuclear Non-Heme Iron Enzymes with the 2-His-1-Carboxylate Facial Triad: Recent Developments in Enzymology and Modeling Studies. *Chem. Soc. Rev.* **2008**, *37*, 2716−2730.

(4) Kovaleva, E. G.; Lipscomb, J. D. Versatility of Biological Non-Heme Fe(II) Centers in Oxygen Activation Reactions. *Nat. Chem. Biol.* **2008**, *4*, 186−193.

(5) Bugg, T. D.; Ramaswamy, S. Non-Heme Iron-Dependent Dioxygenases: Unravelling Catalytic Mechanisms for Complex Enzymatic Oxidations. *Curr. Opin. Chem. Biol.* **2008**, *12*, 134−140.

(6) Davis, K. M.; Altmyer, M.; Martinie, R. J.; Schaperdoth, I.; Krebs, C.; Bollinger, J. M.; Boal, A. K. Structure of a Ferryl Mimic in the Archetypal Iron(II)- and 2-(Oxo)-Glutarate-Dependent Dioxygenase, TauD. *Biochemistry* **2019**, *58*, 4218−4223.

(7) Bollinger, J. M.; Price, J. C.; Hoffart, L. M.; Barr, E. W.; Krebs, C. Mechanism of Taurine: α-Ketoglutarate Dioxygenase (TauD) from Escherichia Coli. *Eur. J. Inorg. Chem.* **2005**, *2005*, 4245−4254.

(8) Hausinger, R. P. Fe(II)/α-Ketoglutarate-Dependent Hydroxylases and Related Enzymes. *Crit. Rev. Biochem. Mol. Biol.* **2004**, *39*, 21−68.

(9) Koehntop, K. D.; Emerson, J. P.; Que, L. J. The 2-His-1-Carboxylate Facial Triad: A Versatile Platform for Dioxygen Activation by Mononuclear Non-Heme Iron(II) Enzymes. *JBIC, J. Biol. Inorg. Chem.* **2005**, *10*, 87−93.

(10) Costas, M.; Mehn, M. P.; Jensen, M. P.; Que, L. J. Dioxygen Activation at Mononuclear Nonheme Iron Active Sites: Enzymes, Models, and Intermediates. *Chem. Rev.* **2004**, *104*, 939−986.

(11) Hegg, E. L.; Que, L. The 2-His-1-Carboxylate Facial Triad - An Emerging Structural Motif in Mononuclear Non-Heme Iron(II) Enzymes. *Eur. J. Biochem.* **1997**, *250*, 625−629.

(12) Valegard, K.; Terwisscha van Scheltinga, A. C.; Lloyd, M. D.; Hara, T.; Ramaswamy, S.; Perrakis, A.; Thompson, A.; Lee, H.-J.; Baldwin, J. E.; Schofield, C. J.; Andersson, J. H.; Anderrson, I. Structure of a Cephalosporin Synthase. *Nature* **1998**, *394*, 805−809.

(13) Elkins, J. M.; Ryle, M. J.; Clifton, I. J.; Dunning Hotopp, J. C.; Lloyd, J. S.; Burzlaff, N. I.; Baldwin, J. E.; Hausinger, R. P.; Roach, P. L. X-Ray Crystal Structure of Escherichia Coli Taurine/α-Ketoglutarate Dioxygenase Complexed to Ferrous Iron and Substrates. *Biochemistry* **2002**, *41*, 5185−5192.

(14) Minor, W.; Steczko, J.; Stec, B.; Otwinowski, Z.; Bolin, J. T.; Walter, R.; Axelrod, B. Crystal Structure of Soybean Lipoxygenase L-1 at 1.4 Å Resolution. *Biochemistry* **1996**, *35*, 10687−10701.

(15) Ha, E. H.; Ho, R. Y. N.; Krisiel, J. F.; Valentine, J. S. Modeling the Reactivity of α-Ketoglutarate-Dependent Non-Heme Iron(II)-Containing Enzymes. *Angew. Chem., Int. Ed.* **1995**, *34*, 2265−2266.

(16) Oldenburg, P. D.; Ke, C. Y.; Tipton, A. A.; Shteinman, A. A.; Que, L. A Structural and Functional Model for Dioxygenases with a 2-His-1-Carboxylate Triad. *Angew. Chem., Int. Ed.* **2006**, *45*, 7975−7978.

(17) Chiou, Y.-M.; Que, L. Models for α-Keto Acid-Dependent Non-Heme Iron Enzymes: Structures and Reactivity of $[\mathrm{Fe^{II}(L)(O_2CCOPh)}](\mathrm{ClO_4})$ Complexes. *J. Am. Chem. Soc.* **1995**, *117*, 3999−4013.

(18) Chiou, Y. M.; Que, L. Model Complexes for α-Keto Acid-Dependent Enzymes. Structure and Reactivity of $\{\mathrm{Fe^{II}}$[Tris[(6-Methyl-2-Pyridyl)Methyl]Amine](Benzoylformate)$\}(\mathrm{ClO_4})$. *J. Am. Chem. Soc.* **1992**, *114*, 7567−7568.

(19) Chiou, Y. -M; Que, L. A Model for α-Keto Acid Dependent Nonheme Iron Enzymes: Structure and Reactivity of $[\mathrm{Fe_2^{II}(Me_2Hdp)_2(Bf)}](\mathrm{ClO_4})$. *Angew. Chem., Int. Ed. Engl.* **1994**, *33*, 1886−1888.

(20) Hagadorn, J. R.; Que, J.; Tolman, W. B. N-Donor Effects on Carboxylate Binding in Mononuclear Iron(II) Complexes of a Sterically Hindered Benzoate Ligand. *Inorg. Chem.* **2000**, *39*, 6086−6090.

(21) Kitajima, N.; Moro-Oka, Y.; Tamura, N.; Amagai, H.; Fukui, H.; Mizutani, Y.; Mathur, R.; Heerwegh, K.; Reed, C. A.; Randall, C. R.; Tatsumi, K. Monomelic Carboxylate Ferrous Complexes as Models for the Dioxygen Binding Sites in Non-Heme Iron Proteins. The Reversible Formation and Characterization of μ-Peroxo Diferric Complexes. *J. Am. Chem. Soc.* **1994**, *116*, 9071−9085.

(22) Bruijnincx, P. C. A.; Lutz, M.; Spek, A. L.; Hagen, W. R.; Weckhuysen, B. M.; Van Koten, G.; Gebbink, R. J. M. K. Modeling the 2-His-1-Carboxylate Facial Triad: Iron-Catecholato Complexes as Structural and Functional Models of the Extradiol Cleaving Dioxygenases. *J. Am. Chem. Soc.* **2007**, *129*, 2275−2286.

(23) Moelands, M. A. H.; Nijsse, S.; Folkertsma, E.; De Bruin, B.; Lutz, M.; Spek, A. L.; Gebbink, R. J. M. K. Bioinspired Nonheme Iron Complexes Derived from an Extended Series of N, N, O-Ligated BAIP Ligands. *Inorg. Chem.* **2013**, *52*, 7394−7410.

(24) Folkertsma, E.; De Waard, E. F.; Korpershoek, G.; Van Schaik, A. J.; Solozabal Mirón, N.; Borrmann, M.; Nijsse, S.; Moelands, M. A. H.; Lutz, M.; Otte, M.; Moret, M. E.; Gebbink, R. J. M. K. Mimicry of the 2-His-1-Carboxylate Facial Triad Using Bulky N, N, O-Ligands: Non-Heme Iron Complexes Featuring a Single Facial Ligand and Easily Exchangeable Co-Ligands. *Eur. J. Inorg. Chem.* **2016**, *2016*, 1319−1332.

(25) Burzlaff, N. Biomimetic Trispyrazolylborato Iron Complexes. *Angew. Chem., Int. Ed.* **2009**, *48*, 5580−5582.

(26) Beck, A.; Weibert, B.; Burzlaff, N. Monoanionic N, N, O-Scorpionate Ligands and Their Iron(II) and Zinc(II) Complexes: Models for Mononuclear Active Sites of Non-Heme Iron Oxidases and Zinc Enzymes. *Eur. J. Inorg. Chem.* **2001**, *2001*, 521−527.

(27) Beck, A.; Barth, A.; Hubner, E.; Burzlaff, N. Bis(Pyrazol-1-Yl)Acetates as Tripodal Heteroscorpionate Ligands in Iron Chemistry: Syntheses and Structures of Iron(II) and Iron(III) Complexes with Bpza, Bdmpza, and Bdtbpza Ligands. *Inorg. Chem.* **2003**, *42*, 7182−7188.

(28) Cappillino, P. J.; Miecznikowski, J. R.; Tyler, L. A.; Tarves, P. C.; McNally, J. S.; Lo, W.; Kasibhatla, B. S. T.; Krzyaniak, M. D.; McCracken, J.; Wang, F.; Armstrong, W. H.; Caradonna, J. P. Studies of Iron(II) and Iron(III) Complexes with Fac-N_2O, Cis-N_2O_2 and N_2O_3 Donor Ligands: Models for the 2-His 1-Carboxylate Motif of Non-Heme Iron Monooxygenases. *Dalt. Trans.* **2012**, *41*, 5662−5677.

(29) Rocks, S. S.; Brennessel, W. W.; Machonkin, T. E.; Holland, P. L. Solid-State and Proton NMR Characterization of an Iron(II) Complex of a Tridentate, Facially Coordinating N, N, O Donor Ligand. *Inorg. Chim. Acta* **2009**, *362*, 1387−1390.

(30) Dhanalakshmi, T.; Bhuvaneshwari, M.; Palaniandavar, M. Iron(III) Complexes of Certain Meridionally Coordinating Tridentate Ligands as Models for Non-Heme Iron Enzymes: The Role of Carboxylate Coordination. *J. Inorg. Biochem.* **2006**, *100*, 1527−1534.

(31) Rittle, J.; Field, M. J.; Green, M. T.; Tezcan, F. A. An Efficient, Step-Economical Strategy for the Design of Functional Metalloproteins. *Nat. Chem.* **2019**, *11*, 434−441.

(32) Liu, J.; Chakraborty, S.; Hosseinzadeh, P.; Yu, Y.; Tian, S.; Petrik, I.; Bhagi, A.; Lu, Y. Metalloproteins Containing Cytochrome, Iron-Sulfur, or Copper Redox Centers. *Chem. Rev.* **2014**, *114*, 4366−4469.

(33) Nastri, F.; Chino, M.; Maglio, O.; Bhagi-Damodaran, A.; Lu, Y.; Lombardi, A. Design and Engineering of Artificial Oxygen-Activating Metalloenzymes. *Chem. Soc. Rev.* **2016**, *45*, 5020−5054.

(34) McLaughlin, M. P.; Retegan, M.; Bill, E.; Payne, T. M.; Shafaat, H. S.; Peña, S.; Sudhamsu, J.; Ensign, A. A.; Crane, B. R.; Neese, F.; Holland, P. L. Azurin as a Protein Scaffold for a Low-Coordinate Nonheme Iron Site with a Small-Molecule Binding Pocket. *J. Am. Chem. Soc.* **2012**, *134*, 19746−19757.

(35) Cavazza, C.; Bochot, C.; Rousselot-Pailley, P.; Carpentier, P.; Cherrier, M. V.; Martin, L.; Marchi-Delapierre, C.; Fontecilla-Camps, J. C.; Ménage, S. Crystallographic Snapshots of the Reaction of

Aromatic C-H with O_2 Catalysed by a Protein-Bound Iron Complex. *Nat. Chem.* **2010**, *2*, 1069−1076.

(36) Snyder, R. A.; Betzu, J.; Butch, S. E.; Reig, A. J.; DeGrado, W. F.; Solomon, E. I. Systematic Perturbations of Binuclear Non-Heme Iron Sites: Structure and Dioxygen Reactivity of de Novo Due Ferri Proteins. *Biochemistry* **2015**, *54*, 4637−4651.

(37) Faiella, M.; Andreozzi, C.; de Rosales, R. T. M.; Pavone, V.; Maglio, O.; Nastri, F.; DeGrado, W. F.; Lombardi, A. An Artificial Di-Iron Oxo-Protein with Phenol Oxidase Activity. *Nat. Chem. Biol.* **2009**, *5*, 882−884.

(38) Wilson, M. E.; Whitesides, G. M. Conversion of a Protein to a Homogeneous Asymmetric Hydrogenation Catalyst by Site-Specific Modification with a Diphosphinerhodium(I) Moiety. *J. Am. Chem. Soc.* **1978**, *100*, 306−307.

(39) Ward, T. R. Artificial Metalloenzymes Based on the Biotin-Avidin Technology: Enantioselective Catalysis and Beyond. *Acc. Chem. Res.* **2011**, *44*, 47−57.

(40) Schwizer, F.; Okamoto, Y.; Heinisch, T.; Gu, Y.; Pellizzoni, M. M.; Lebrun, V.; Reuter, R.; Köhler, V.; Lewis, J. C.; Ward, T. R. Artificial Metalloenzymes: Reaction Scope and Optimization Strategies. *Chem. Rev.* **2018**, *118*, 142−231.

(41) Heinisch, T.; Ward, T. R. Artificial Metalloenzymes Based on the Biotin-Streptavidin Technology: Challenges and Opportunities. *Acc. Chem. Res.* **2016**, *49*, 1711−1721.

(42) Mann, S. I.; Heinisch, T.; Weitz, A. C.; Hendrich, M. P.; Ward, T. R.; Borovik, A. S. Modular Artificial Cupredoxins. *J. Am. Chem. Soc.* **2016**, *138*, 9073−9076.

(43) Mann, S. I.; Heinisch, T.; Ward, T. R.; Borovik, A. S. Peroxide Activation Regulated by Hydrogen Bonds within Artificial Cu Proteins. *J. Am. Chem. Soc.* **2017**, *139*, 17289−17292.

(44) Olshansky, L.; Huerta-Lavorie, R.; Nguyen, A. I.; Vallapurackal, J.; Furst, A.; Tilley, T. D.; Borovik, A. S. Artificial Metalloproteins Containing Co_4O_4 Cubane Active Sites. *J. Am. Chem. Soc.* **2018**, *140*, 2739−2742.

(45) Skander, M.; Humbert, N.; Collot, J.; Gradinaru, J.; Klein, G.; Loosli, A.; Sauser, J.; Zocchi, A.; Gilardoni, F.; Ward, T. R. Artificial Metalloenzymes: (Strept)Avidin as Host for Enantioselective Hydrogenation by Achiral Biotinylated Rhodium-Diphosphine Complexes. *J. Am. Chem. Soc.* **2004**, *126*, 14411−14418.

(46) Andersen, O. A.; Flatmark, T.; Hough, E. High Resolution Crystal Structures of the Catalytic Domain of Human Phenylalanine Hydroxylase in Its Catalytically Active Fe(II) Form and Binary Complex with Tetrahydrobiopterin. *J. Mol. Biol.* **2001**, *314*, 279−291.

(47) Groom, C. R.; Bruno, I. J.; Lightfoot, M. P.; Ward, S. C. The Cambridge Structural Database. *Acta Crystallogr., Sect. B: Struct. Sci., Cryst. Eng. Mater.* **2016**, *72*, 171−179.

(48) Hirata, K.; Shinzawa-Itoh, K.; Yano, N.; Takemura, S.; Kato, K.; Hatanaka, M.; Muramoto, K.; Kawahara, T.; Tsukihara, T.; Yamashita, E.; Tono, K.; Ueno, G.; Hikima, T.; Murakami, H.; Inubushi, Y.; Yabashi, M.; Ishikawa, T.; Yamamoto, M.; et al. Determination of Damage-Free Crystal Structure of an X-Ray-Sensitive Protein Using an XFEL. *Nat. Methods* **2014**, *11*, 734−736.

(49) Suga, M.; Akita, F.; Hirata, K.; Ueno, G.; Murakami, H.; Nakajima, Y.; Shimizu, T.; Yamashita, K.; Yamamoto, M.; Ago, H.; Shen, J.-R. Native Structure of Photosystem II at 1.95 Å Resolution Viewed by Femtosecond X-Ray Pulses. *Nature* **2015**, *517*, 99−103.

(50) Kern, J.; Yachandra, V. K.; Yano, J. Metalloprotein Structures at Ambient Conditions and in Real-Time: Biological Crystallography and Spectroscopy Using X-Ray Free Electron Lasers. *Curr. Opin. Struct. Biol.* **2015**, *34*, 87−98.

(51) Kern, J.; Tran, R.; Alonso-Mori, R.; Koroidov, S.; Echols, N.; Hattne, J.; Ibrahim, M.; Gul, S.; Laksmono, H.; Sierra, R. G.; Gildea, R. J.; Han, G.; Hellmich, J.; Lassalle-Kaiser, B.; Chatterjee, R.; Brewster, A. S.; Stan, C. A.; Glöckner, C.; et al. Taking Snapshots of Photosynthetic Water Oxidation Using Femtosecond X-Ray Diffraction and Spectroscopy. *Nat. Commun.* **2014**, *5*, 4371.

(52) Mcdonald, A. R.; Bukowski, M. R.; Farquhar, E. R.; Jackson, T. A.; Koehntop, K. D.; Seo, M. S.; Hont, R. F. De; Stubna, A.; Halfen, J. A.; Mu, E. Sulfur versus Iron Oxidation in an Iron - Thiolate Model Complex. *J. Am. Chem. Soc.* **2010**, *132* (4), 17118−17129.

(53) England, J.; Farquhar, E. R.; Guo, Y.; Cranswick, M. A.; Ray, K.; Eckard, M.; Que, L. Characterization of a Tricationic Trigonal Bipyramidal Iron(IV) Cyanide Complex, with a Very High Reduction Potential, and Its Iron(II) and Iron(III) Congeners. *Inorg. Chem.* **2011**, *50* (7), 2885−2896.

(54) Rohde, J.; Shan, X.; Lim, M. H.; Klinker, E. J.; Chen, K.; Nam, W.; Que, L. Structural Insights into Nonheme Alkylperoxoiron(III) and Oxoiron(IV) Intermediates by X-ray Absorption Spectroscopy. *J. Am. Chem. Soc.* **2004**, *126* (51), 16750−16761.

(55) Berry, J. F.; Bill, E.; Bothe, E.; Weyhermüller, T.; Wieghardt, K. Octahedral Non-Heme Non-Oxo Fe(IV) Species Stabilized by a Redox-Innocent N-Methylated Cyclam-Acetate Ligand. *J. Am. Chem. Soc.* **2005**, *127*, 11550−11551.

(56) Grapperhaus, C. A.; Mienert, B.; Bill, E.; Weyhermüller, T.; Wieghardt, K. Mononuclear (Nitrido)Iron(V) and (Oxo)Iron(IV) Complexes via Photolysis of $[(\text{Cyclam-Acetato})\text{Fe}^{\text{III}}(\text{N}_3)]^+$ and Ozonolysis of $[(\text{Cyclam-Acetato})\text{Fe}^{\text{III}}\text{O}_3\text{SCF}_3)]^+$ Water/Acetone Mixtures. *Inorg. Chem.* **2000**, *39*, 5306−5317.

(57) Pangborn, A. B.; Giardello, M. A.; Grubbs, R. H.; Rosen, R. K.; Timmers, F. J. Safe and Convenient Procedure for Solvent Purification. *Organometallics* **1996**, *15*, 1518−1520.

(58) Chambers, J. M.; Lindqvist, L. M.; Webb, A.; Huang, D. C. S.; Savage, G. P.; Rizzacasa, M. A. Synthesis of Biotinylated Episilvestrol: Highly Selective Targeting of the Translation Factors EIF4AI/II. *Org. Lett.* **2013**, *15*, 1406−1409.

(59) Incarvito, C.; Lam, M.; Rhatigan, B.; Rheingold, A. L.; Qin, C. J.; Gavrilova, A. L.; Bosnich, B. Bimetallic Reactivity. Preparations, Properties and Structures of Complexes Formed by Unsymmetrical Binucleating Ligands Bearing 4- and 6-Coordinate Sites Supported by Alkoxide Bridges. *J. Chem. Soc. Dalt. Trans.* **2001**, No. 23, 3478−3488.

(60) Baffert, C.; Romero, I.; Jacques, P.; Deronzier, A. Synthesis and Structural Characterization of Five-, Six-, and Seven-Coordinate Mononuclear Manganese (II) Complexes with N -Tridentate Ligands. *Inorg. Chim. Acta* **2004**, *357*, 3430−3436.

(61) Mukherjee, J.; Balamurugan, V.; Gupta, R.; Mukherjee, R. Synthesis and Properties of Fe^{III} and Co^{III} Complexes: Structures of $[(\text{L}^2)\text{Fe}(\text{N}_3)_3]$, $[(\text{L}^2)_2\text{Fe}_2(\mu\text{-O})(\mu\text{-O}_2\text{CMe})_2][\text{ClO}_4]_2\cdot 2\text{H}_2\text{O}$ and $[(\text{L}^2)_2\text{Co}_2(\mu\text{-OH})_2(\mu\text{-O}_2\text{CMe})][\text{ClO}_4]_3\cdot\text{MeCN}$ [L^2 = methyl[2-(2-pyridyl)ethyl](2-pyridylmethyl)amine]. *Dalton Trans.* **2003**, 3686−3692.

(62) Petasis, D. T.; Hendrich, M. P. Quantitative Interpretation of Multifrequency Multimode EPR Spectra of Metal Containing Proteins, Enzymes, and Biomimetic Complexes. *Methods Enzymol.* **2015**, *563*, 171−208.